The Impact of Southern Ocean Topographic Barriers on the Ocean Circulation and the Overlying Atmosphere

Agatha M. de Boer,[a] David K. Hutchinson,[a,b] Fabien Roquet,[c] Louise C. Sime,[d] Natalie J. Burls,[e] and Céline Heuzé[f]

[a] Department of Geological Sciences, Stockholm University, Stockholm, Sweden
[b] Climate Change Research Centre, University of New South Wales Sydney, Sydney, Australia
[c] Department of Marine Sciences, University of Gothenburg, Göteborg, Sweden
[d] British Antarctic Survey, Cambridge, United Kingdom
[e] Department of Atmosphere, Ocean and Earth Science, George Mason University, Fairfax, Virginia
[f] Department of Earth Sciences, University of Gothenburg, Göteborg, Sweden

ABSTRACT: Southern Ocean bathymetry constrains the path of the Antarctic Circumpolar Current (ACC), but the bathymetric influence on the coupled ocean–atmosphere system is poorly understood. Here, we investigate this impact by respectively flattening large topographic barriers around the Kerguelen Plateau, Campbell Plateau, Mid-Atlantic Ridge, and Drake Passage in four simulations in a coupled climate model. The barriers impact both the wind and buoyancy forcing of the ACC transport, which increases by between 4% and 14% when barriers are removed individually and by 56% when all barriers are removed simultaneously. The removal of Kerguelen Plateau bathymetry increases convection south of the plateau and the removal of Drake Passage bathymetry reduces convection upstream in the Ross Sea. When the barriers are removed, zonal flattening of the currents leads to sea surface temperature (SST) anomalies that strongly correlate to precipitation anomalies, with correlation coefficients ranging between $r = 0.92$ and $r = 0.97$ in the four experiments. The SST anomalies correlate to the surface winds too in some locations. However, they also generate circumpolar waves of sea level pressure (SLP) anomalies, which induce remote wind speed changes that are unconnected to the underlying SST field. The meridional variability in the wind stress curl contours over the Mid-Atlantic Ridge, the Kerguelen Plateau, and the Campbell Plateau disappears when these barriers are removed, confirming the impact of bathymetry on surface winds. However, bathymetry-induced wind changes are too small to affect the overall wave-3 asymmetry in the Southern Hemisphere westerlies. Removal of Southern Hemisphere orography is also inconsequential to the wave-3 pattern.

SIGNIFICANCE STATEMENT: Several studies in the past have pointed to the controlling effect of bathymetry on currents in the Southern Ocean circulation, but a clear idea of the importance of the major topographic barriers in the Southern Ocean is lacking. By removing these barriers systematically in a coupled climate model, we can evaluate their impact on several important components of the climate system, such as the Antarctic Circumpolar Current (ACC) pathways and strength, Antarctic Bottom Water formation, sea surface temperature, overlying winds, air–sea fluxes, and even precipitation. This helps in our understanding of what controls the pathways of the ACC and how much it matters for climate.

Authors Agatha M. de Boer and David K. Hutchinson contributed equally to the manuscript.

Corresponding author: Agatha de Boer, agatha.deboer@geo.su.se

1. Introduction

The bathymetry of the Southern Ocean is complex with several major topographic barriers linked together by interconnected ridges. The fundamental impact that the Southern Ocean topography has on its circulation patterns has long been recognized. The existence of an open band of latitude across Drake Passage allows the Antarctic Circumpolar Current (ACC) to flow around the globe unimpeded by continents (e.g., Rintoul 2018). The ACC connects water masses from all major ocean basins of the World Ocean, making it a central

element of the global overturning circulation (e.g., Cessi 2019). The zonal structure of the ACC isolates the Antarctic continent effectively from the rest of the globe, thereby contributing toward making it the coldest place on Earth (Martinson 2012). The ACC has an equivalent barotropic vertical structure with an *e*-folding vertical scale of about 1000 m (Killworth and Hughes 2002), meaning that its surface flow is strongly affected by topographic features shallower than roughly 3-km depth. Along its path, several major barriers must be crossed including several ridges within the Drake Passage, the mid-Atlantic ridge, the Kerguelen Plateau, and the Campbell Plateau. A quick examination of the main ACC pathways reveals the strong constraint imposed by topographic barriers on the flow. However, the details of how the bathymetry influences winds, sea surface temperature (SST), and currents in the Southern Ocean is complex and remains poorly characterized.

The winds, SST, and currents all influence and are influenced by each other, making it complicated to identify the direct effect of the topography on the ocean circulation and the overlying atmosphere in coupled models. For example, the strength of the Antarctic Circumpolar Current is affected by the intensity and position of the overlying Southern Hemisphere (SH) westerlies (Allison et al. 2010; Langlais et al. 2015). However, the impact of the wind on the ACC transport is not straightforward but modulated by the eddy field, stratification, and bathymetry (Bishop et al. 2016; Fyfe and Saenko 2005; Hogg 2010; Patmore et al. 2019; Zika et al. 2013). The momentum input of the westerly wind is approximately cancelled by the bottom form stress caused by barriers in the path of the ACC (Gille 1997; Johnson and Bryden 1989; Stevens and Ivchenko 1997). The bathymetry also controls the number of fronts that make up the ACC at a given longitude as well as their latitudinal position (de Boer et al. 2013b; Graham et al. 2012; Marshall 1995; Sokolov and Rintoul 2007; Tansley and Marshall 2000, 2001; Thompson 2010). [Note that in this work, the term *fronts* is used to indicate dynamical fronts associated with currents, and not the circumpolar fronts associated with definitions related to temperature and salinity contours (Graham and de Boer 2013).] In turn, the path of ACC fronts influences oceanic heat transport and therefore the ocean temperature field, and so by extension one would expect the bathymetry to influence the SST field. Yet, the SST field can affect the strength and latitudinal position of the westerlies (Sime et al. 2013, 2016), as well as western boundary current storms and the SH storm tracks (Czaja and Blunt 2011; de Boer et al. 2013a; Inatsu and Hoskins 2004). Winds are also altered locally by SST because the atmospheric layer above cold water is more stable than that above warm water so that the wind speeds decrease more rapidly over colder water (Chelton et al. 2004; Small et al. 2008). With this mechanism, strong local SST gradients, such as that associated with dynamic fronts in the ACC, can induce an overlying zero wind stress curl (de Boer et al. 2013b; Graham et al. 2012; Pauthenet et al. 2017).

The role of SO bathymetry on the ocean and climate state has been studied extensively, although usually with a focus on the impact of an open circumpolar connection on the meridional overturning circulation and the isolation of Antarctica from warm equatorward-flowing waters (Elsworth et al. 2017;

Goldner et al. 2014; Hutchinson et al. 2019, 2021; Katz et al. 2011; Sijp et al. 2011; Toggweiler and Samuels 1995; Toumoulin et al. 2020; Viebahn et al. 2016; Yang et al. 2014). In such studies, the Drake Passage or Tasman Gateway is usually closed to various extents and the resulting simulations compared with one that has gateways more similar to today. One important exception is the study of Wang et al. (2016) in which the Kerguelen Plateau was removed. The authors calculated that the plateau bears 16% of the form stress of the ACC but this was simply redistributed among the other barriers when the plateau was removed, without much impact on the ACC strength. Given that the experiments were performed in an ocean-only model with restoring to a prescribed SST climatology, the study was not appropriate for evaluating the role of the plateau on SST or the overlying atmosphere.

The alteration of the SO bathymetry in a coupled atmosphere–ocean–ice model provides a method by which to isolate the impact of topography on currents, of currents on SST, and of the SST on the overlying atmosphere. It also provides a way to elucidate potential errors made when simplifying the bathymetric features in the Southern Ocean in idealized or low-resolution climate models, process models, and paleoclimate simulations of deep past periods where bathymetric features are often uncertain. Here, we perform such a study by running a coupled climate model in which we remove the four major topographic barriers in the Southern Ocean. These are the Drake Passage ridges (South Georgia and South Sandwich Islands), the Kerguelen Plateau, the Campbell plateau, and the Mid-Atlantic Ridge. The model and simulations are described in section 2. In section 3 we present the effect of the barriers on the ocean and in particular the currents, SST, ACC strength, and AABW formation. In section 4 we discuss the impact on the atmosphere and in particular the precipitation and winds. Finally, we present our conclusions and consider the shortcomings of the study in section 5.

2. Experimental design

We used the coupled climate model GFDL CM2.1 to investigate the role of the topographic barriers in the Southern Ocean (Delworth et al. 2006). The atmosphere model, land model, and sea ice models are the same as in CM2.1, while the ocean's component has been updated to MOM version 5.1.0. The ocean and sea ice models have a horizontal resolution of 1° latitude × 1° longitude and the ocean has 50 vertical levels. There is a progressive increase in latitudinal resolution from 1° in the extratropics to 0.33° equatorward of 30° latitude. The ocean grid has a regular latitude–longitude spacing south of 65°N and a bipolar grid north of this latitude (Hutchinson et al. 2018; Murray 1996). The atmospheric model has a horizontal resolution of 2° latitude × 2.5° longitude and 24 vertical levels. Note that this version of the model differs from that of Hutchinson et al. (2018), who used a resolution of 1° × 1.5° in the ocean and 3° × 3.75° atmosphere model. The choice here was made to align with the original CM2.1 model, which was tuned to reproduce an accurate preindustrial climate, and meridional overturning circulation that aligns with observations. This resolution does not permit a detailed study of the role of fronts
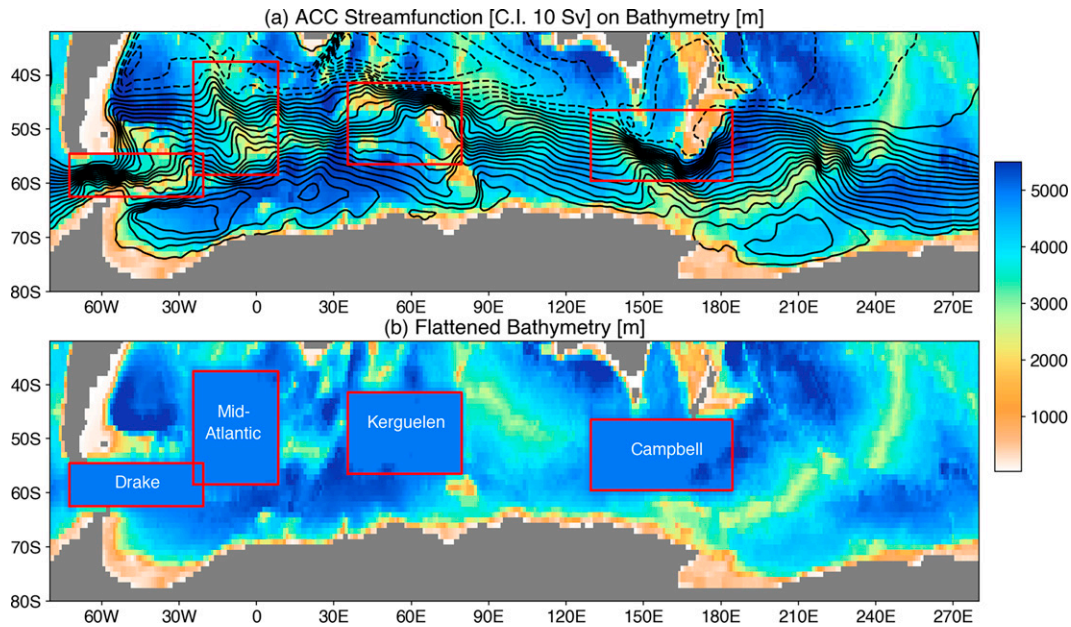
FIG. 1. (a) Contours of the barotropic streamfunction of the Antarctic Circumpolar Current (interval 10 Sv) and the bathymetry in the control simulation. (b) The four areas that were flattened to 5000-m depth (with some smoothing at the edges) in the four sensitivity experiments are indicated in the red squares.

and eddies but allows for the longer simulations needed to get the deep ocean in quasi-equilibrium. We evaluate the realism in the flow by comparing one year (2020 in this case) of SSH gridded data from satellite observations (Taburet et al. 2019) to the SSH in the final year of our control simulation (see Fig. S1 in the online supplemental material). As expected, the flow field is smoother in our model, although the main path of the SSH contours is similar, swerving around the bathymetric features to conserve potential vorticity. The veering of the contours around the Mid-Atlantic ridge appears less pronounced in the observations than the model, suggesting that the impact of the removal of this barrier may be exaggerated in this study.

The model uses the Bryan–Lewis vertical mixing scheme (Bryan and Lewis 1979), using the following parameters:

$$K_{eq}(z) = 10^{-4} \left\{ 0.65 + \frac{1.15}{\pi} \tan^{-1}[4.5 \times 10^{-3}(z - 2500)] \right\},$$

$$K_{pole}(z) = 10^{-4} \left\{ 0.75 + \frac{0.95}{\pi} \tan^{-1}[4.5 \times 10^{-3}(z - 2500)] \right\},$$

where K_{eq} and K_{pole} are the equatorial and polar diffusivities ($m^2 \, s^{-1}$), respectively. The depth z is in meters, which has a transition level at 2500 m as shown above. The low latitudes use K_{eq} and the high latitudes use K_{pole}, with a transition at 35° latitude. In addition to this background mixing, surface mixing is enhanced using the k-profile parameterization scheme, as described in Griffies et al. (2005). The isopycnal mixing and eddy parameterization are implemented using the Redi and Gent–McWilliams schemes, as formulated in Griffies (1998). In keeping with the CM2.1 model formulation, we use the same parameters for the Redi and Gent–McWilliams mixing

schemes as described in Griffies et al. (2005). The model uses parameterized lateral mixing to connect marginal seas to the global ocean, in regions where the grid resolution is insufficient to allow flow through narrow straits. These marginal seas are Hudson Bay, the Black Sea, the Mediterranean Sea, the Red Sea, the Baltic Sea, and the Persian Gulf.

All of the simulations are initialized using an observational dataset of ocean temperature and salinity from Steele et al. (2001), as described in Delworth et al. (2006). Greenhouse gas, aerosol, and orbital forcing parameters are set at year 1860 levels (i.e., preindustrial conditions). The forcing is thus from a period more than 100 years earlier than the initial conditions, but this should not play a major role given that the simulation are 1500 years long. However, we do check that our simulations are in equilibrium and the results do not depend on the exact averaging time.

In each of the four sensitivity experiments, a major topographic barrier and its surrounding area was flattened to a depth of 5000 m. (Fig. 1; Table 1). In the "Drake" experiment, the South Georgia and South Sandwich Islands were removed. For the "Mid-Atlantic" experiment, the ridge was

TABLE 1. The flattened regions of each perturbation experiment. The ocean depth was set to 5000 m in the region between X_0 and X_1, in longitude space, and between Y_0 and Y_1 in latitude space.

Experiment	X_0	X_1	Y_0	Y_1
Drake	−72.5	−20.5	−62.5	−54.5
Mid-Atlantic	−24.5	8.5	−58.7	−37.5
Kerguelen	35.5	80.5	−56.5	−41.5
Campbell	129.5	184.5	−59.5	−46.5

flattened between 37° and 58°S. The "Kerguelen" experiment has the Kerguelen Plateau north of 56°S flat as well as the Del Caño Rise and the Conrad Rise to its west. Finally, in the "Campbell" experiment, the topography south of Australia and New Zealand down to 60°S was flattened, including the Campbell Plateau, the Macquarie Ridge, and the South Tasman Rise. The latitude and longitude limits of the flattened region in each case are given in Table 1. At the edge of the flattened region, the depth in a two grid-cell "halo" was linearly interpolated between the flat region (5000 m) and the adjacent grid cell depth outside the halo. This halo provides a smoothing of any sharp gradients in bathymetry that may have been created at the edges of the flattened regions. In addition to these core simulations, we performed one simulation where all four barriers were removed (referred to as "All"), and three simulations where the orography of South America, Australia/New Zealand, and Antarctica was flattened south of 30°S, respectively. These last three experiments are briefly referred to in connection to the wave-3 pattern of Southern Hemisphere westerlies in section 4b(2) and named Andes, Aus NZ, and Antarc flat, respectively.

All simulations have been run for 1500 years from initial conditions. This is not enough for a full equilibrium of deep ocean temperature and salinity, but it is enough to distinguish between fast and slow processes that are affected by the removal of the topography. The analyses and figures presented here are from the average of the last 100 years of each simulation (i.e., years 1400–1500). In several instances, we have also checked the results at earlier periods and for longer averaging times and in those cases, it is explicitly mentioned.

3. The impact of barriers in the ocean

a. Currents

The number and strength of the fronts in the ACC path vary with longitude and can be anything from 0 to 10, though this depends on how a front is defined (Graham et al. 2012). The latitudinal position of the fronts is tightly coupled to the bathymetry, as they swerve around topographic obstacles to conserve their potential vorticity (Graham et al. 2012; Marshall 1995). The removal of these obstacles in the path of the ACC leads therefore to a zonal flattening of the fronts and the local streamlines (Fig. 2). In the Drake experiment, the currents on the northern side of the passage increase and flow horizontally over the areas previously occupied by the East Scotia Ridge (Figs. 2c,d). This increase is mostly compensated with a decrease of the current on the southern flank of Drake Passage, while the northward flowing Malvinas Current decreases only mildly. In the Mid-Atlantic experiment, the removal of the ridge causes a flow anomaly predominantly in the region of the changed bathymetry (Figs. 2e,f). In the control simulation, the northern fronts of the ACC (associated with the part of the ACC that flows northward in the Malvinas currents after Drake Passage) moves either north or south around the Mid-Atlantic ridge and when this ridge is removed, it flows straight across. The removal of the Kerguelen Plateau leads to a similar change in that currents that diverge around the barrier in the

control run now flow zonally across this region (Fig. 2h). Since the plateau is wider and shallower and more central in the ACC flow field, the flow anomaly is somewhat larger than in the case of Mid-Atlantic case. Finally, in the Campbell experiment, the removal of the plateau barrier allows the ACC to flow zonally across this region (Figs. 2i,j). This was not obvious a priori, since the westerly winds here turn southward so that the current may have diverged southward regardless of its now open path to the east, to utilize the momentum of the winds (Allison et al. 2010).

All experiments exhibit some upstream and downstream adjustments to the flow field. The largest nonlocal adjustments are found in the Drake experiments where the northward shift in the transport through Drake Passage affects the flow upstream in the whole Pacific sector of the Southern Ocean, including the disappearance of the Ross Gyre. Some upstream and downstream affects are to be expected; in the coupled climate model study of Graham et al. (2012), they suggested that the fronts in the Pacific sector of the Southern Ocean, which did not react to climate change, were controlled by upstream and downstream topography. In a more purpose-built study, Tansley and Marshall (2001) investigated the impact of topography downstream of Drake Passage (representing Kerguelen Plateau in their case) on the Southern Ocean flow field in a so-called "geostrophic vorticity" model with simplified geometry. They performed many sensitivity studies with different downstream bathymetries and found that the bathymetry influenced the structure and stability of the time-mean circulation in all cases, but that the nature of the change was difficult to predict, even in that simple model. It is therefore not expected that the nature of upstream or downstream changes in the flow field in the more physically and geographically complicated model used here would be predictable or self-evident.

b. Sea surface temperature

When the ACC meanders around a topographic obstacle, it leads to anomalous meridional flow. If the flow is going northward, the cold polar waters from the south cause anomalously cold conditions in comparison to the zonal mean and, conversely, if the flow is southward, it creates warm conditions. This can be seen clearly at the Mid-Atlantic ridge where the 8°C SST contour in the control simulation (and other simulations where the ridge is present) shifts northward and the 4°C contour shifts southward around the ridge (Fig. 3; 5°–20°W). When the ridge is removed, in the Mid-Atlantic experiments, both these contours are more zonal. In the Indian Ocean sector of the Southern Ocean, the divergence of the flow around the Del Caño Rise, Conrad Rise, and the northern and southern Kerguelen plateaus leads to large meridional excursions of the temperature contours, which flatten when the barriers are removed (Fig. 3; 60°–90°E). Similarly, the Campbell plateau causes a southward deflection of the 2°, 4°, and 8°C contours (Fig. 3; 160°E–180°) and the fracture zones between Australia and Antarctica lead to a northward deflection of the 2° and 4°C contours (Fig. 3; 140°–160°E). In the Drake Passage case, the topographic barriers lead to more ACC transport entering the passage on its southern flank, thus forcing the ACC fronts
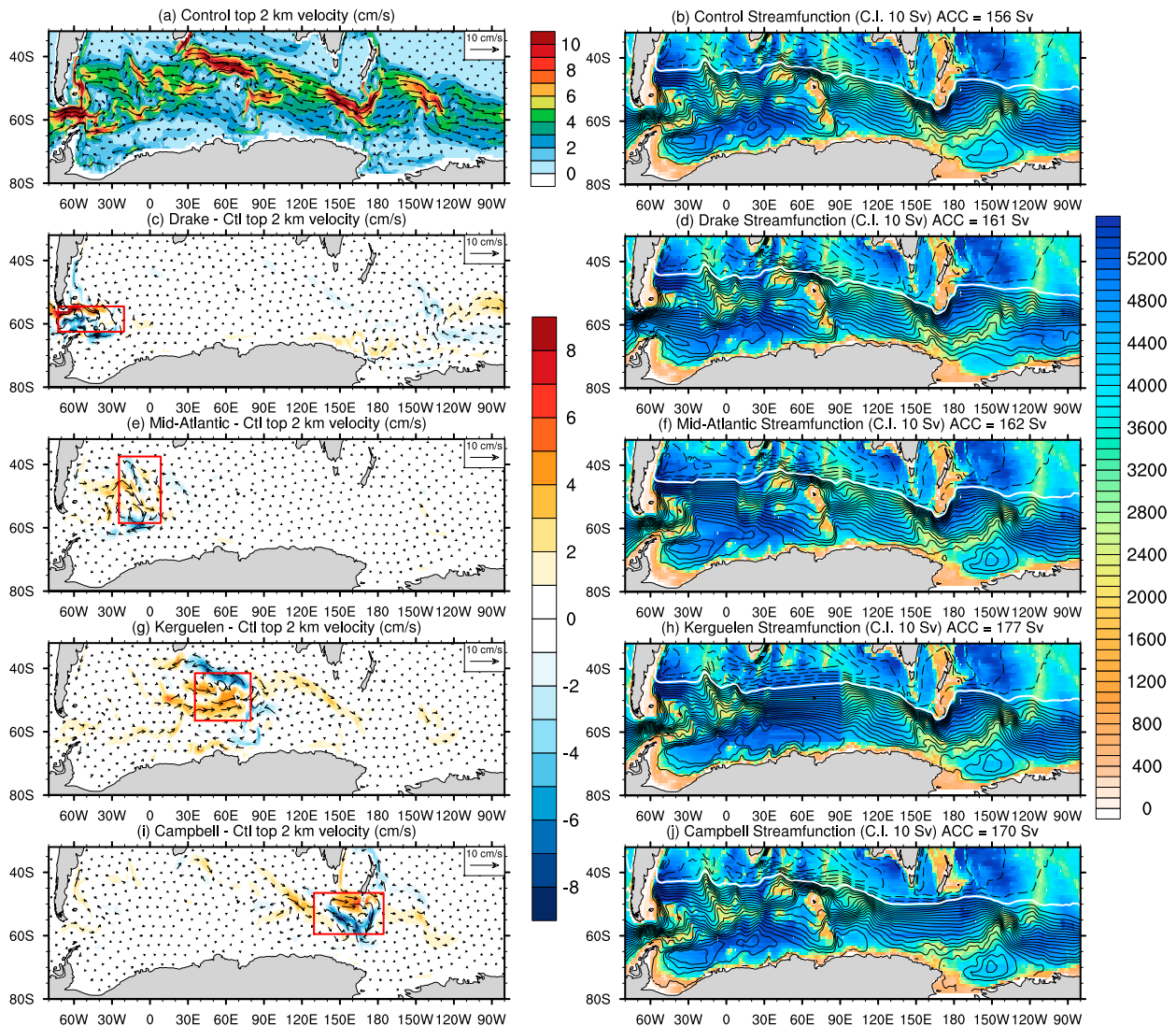
FIG. 2. (a) The control experiment ocean currents averaged over the top 2 km and (b) the barotropic streamfunction. (left) The top 2-km layer current anomalies from the control and (right) the barotropic streamlines for the four experiments where major bathymetric features are removed: (c),(d) Drake, (e),(f) Mid-Atlantic, (g),(h) Kerguelen, and (i),(j) Campbell. The colors on the left represent the changes in the speed of the currents so that positive and negative anomalies respectively indicate that the current has sped up or slowed down. The arrows indicate the anomalous velocity. Red boxes show the regions where barriers were removed. Colors on the right indicate the depth of the bathymetry (in m).

in the South Pacific southward and warming the South Pacific upstream of the passage. The removal of the Drake Passage topography thus leads to a northward movement of the 2° and 4°C SST contours upstream of the passage.

The spatial warming and cooling patterns described above can be seen in the SST difference plots between the four experiments and the control simulation (Fig. 4, left). It is evident that the warming and cooling anomalies are mostly local to the underwater barriers, with some notable exceptions. SST anomalies related to flow meandering upstream of the obstacles are visible in the South Pacific in the Drake experiment (Fig. 4b) and in the Agulhas retroflection region south of South Africa in the Kerguelen experiment (Fig. 4g). In these

cases, the SST changes can be coupled to the upstream and downstream changes in the flow field as discussed in the previous section. For example, the SST upstream of Drake Passage decreases in the Drake experiment, as the southeastward flow of warmer subtropical water from the Mid-Pacific Rise (~145°W) turns more zonal to feed the northern part of Drake Passage (Figs. 2c,d and 4c).

c. Strength of the ACC

The momentum input from the wind stress is almost all balanced by bottom form stress at shallow topographic features (<3700 m) while the form stress at the bottom in deeper waters comprises eastward and westward form stress that balance
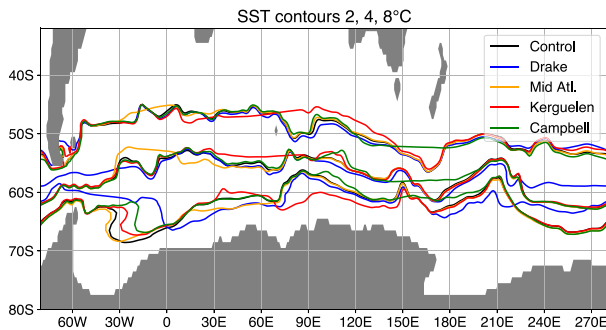
SST contours 2, 4, 8°C

FIG. 3. The 2°, 4°, and 8°C SST contours in the control and the four perturbation experiments, where the 2°C contours are the most southern ones.

in the zonal integral (Gille 1997; Masich et al. 2015). The Kerguelen Plateau, the South American continent, and the Macquarie Ridge are thought to be the major sinks of westward momentum (Gille 1997; Masich et al. 2015). In our simulations, we also find that the removal of the barriers in the Kerguelen and Campbell (including Macquarie Ridge) experiments leads to the largest increases in the ACC (~14% and 10%, respectively; Table 2). The increases in the ACC in the Drake and Mid-Atlantic experiments are less than 6% and this is not significant given that the 100-yr mean ACC transport in the Control simulation is still trending upward slightly after 1500 years (Fig. 5).

The ACC transport decreases initially in all experiments in the first 200 years, after which it regains strength. In our simulations, we cannot determine the adjustment time for the ACC transport from the topographic changes directly, because all the simulations are initiated from the same cold start. This implies that the initial ACC changes are dominated by the general adjustment of the simulations to reach a quasi-equilibrium state in which the atmosphere and ocean is in balance. However, when the Kerguelen Plateau was removed in the ocean-only simulation of Wang et al. (2016), they found that form stress was redistributed between the remaining barriers within about 50 days, while the ACC transport changed on slower decadal time scales. It is therefore reasonable to assume similar adjustment time scales here for the form stress and the ACC transport, except that the simulations here may have feedbacks from the atmosphere on longer time scales, not present in an ocean-only model. However, as we discuss in sections 4b and 5, while there is considerable interannual and multidecadal variability in the wind field, the major features of its response to the topography are already present in the first few decades so we do not expect the long-term atmospheric feedback on the ACC to be significant. Assuming then that the role of the adjustment to a new distribution of form stress occurs in the first year similar to Wang et al. (2016), that implies the rest of the variability of the ACC is due to the slower adjustment of the stratification to the buoyancy forcing—in other words, the baroclinic forcing from the meridional density gradients across the ACC that is focused in the upper 2000 m (Shi et al. 2020). As we can see in Fig. 5, the ACC in some of the simulations (e.g., Drake) appears closer to

equilibrium after 1500 years than others (e.g., Control). The apparent difference in adjustment time scales of the ACC could be due to the different pathways it takes in the experiments, which would subject it to different wind and buoyancy forcing. The pathways also affect the variability of the ACC; for example, the ACC transport during the last 300 years fluctuates between 146 and 163 Sv (a range of 17 Sv; 1 Sv $\equiv 10^6$ m^3 s^{-1}) in the control simulation, but between 145 and 180 Sv (a range of 34 Sv) when the Mid-Atlantic Ridge is removed (Table 2; Fig. 5).

As seen, the removal of any individual barrier does not have a large effect, suggesting that much of the bottom stress gets merely distributed elsewhere without a strong ACC transport change. However, if the four barriers are removed simultaneously (not shown), then the ACC increases by 88 Sv or 56%, which is much higher than the linear sum of the individual effects of these barriers (i.e., 46 Sv or 30%). The importance of individual barriers on the ACC transport depends therefore on the availability of other barriers to take up the lost form stress.

d. Antarctic Bottom Water formation

There are several reasons why the topographic barriers in the Southern Ocean may influence Antarctic Bottom Water (AABW) formation. The topographic barriers promote net zonal pressure gradients, which are required to sustain a net meridional geostrophic flow. As such they allow for the return and upwelling of North Atlantic Deep Water in the Southern Ocean as well as the exit of AABW from the Southern Ocean. Removing some of these barriers would thus likely change the pathways of AABW to the rest of the world. As we have seen, the barriers also alter the zonal flow patterns, as they force fronts to pass southward or northward of the obstacle. Meandering in the ACC is known to increase southward eddy heat fluxes (Dufour et al. 2015; Newsom et al. 2021) so that one would expect the meridional excursions of the flow to increase poleward heat transport. The strength of the ACC is also tightly linked to that of the subpolar gyres: strong gyres cause dynamic and thermodynamic stresses on the sea ice and hence increase the likelihood of open ocean polynyas, in which open ocean deep convection (and hence AABW formation) can take place (Zhou et al. 2022). The changes in the meridional and zonal flow should also affect the water mass properties in the Southern Ocean with a potential knock-on effect on AABW formation. In turn, AABW formation has been repeatedly shown to accelerate the subpolar gyres, and hence the ACC (Cheon et al. 2014; Martin et al. 2013).

Here, the impact of the barriers on AABW formation is primarily investigated by evaluating changes in the Southern Ocean mixed layer depth (MLD) when removing the barriers. Although in the "real" present-day Southern Ocean deep convection does not contribute significantly to AABW formation, observations suggest that it was a large contributor until the 1950s (Broecker et al. 1999). In the Control simulation, the deepest MLDs are found in the area of the Weddell Sea and Ross Sea (Fig. 6a). The maximum MLD in the Weddell Sea is about 1750 m at ~68°S, 30°W, and in the Ross Sea the maximum is about 600 m at ~70°S, 180°W, where values are
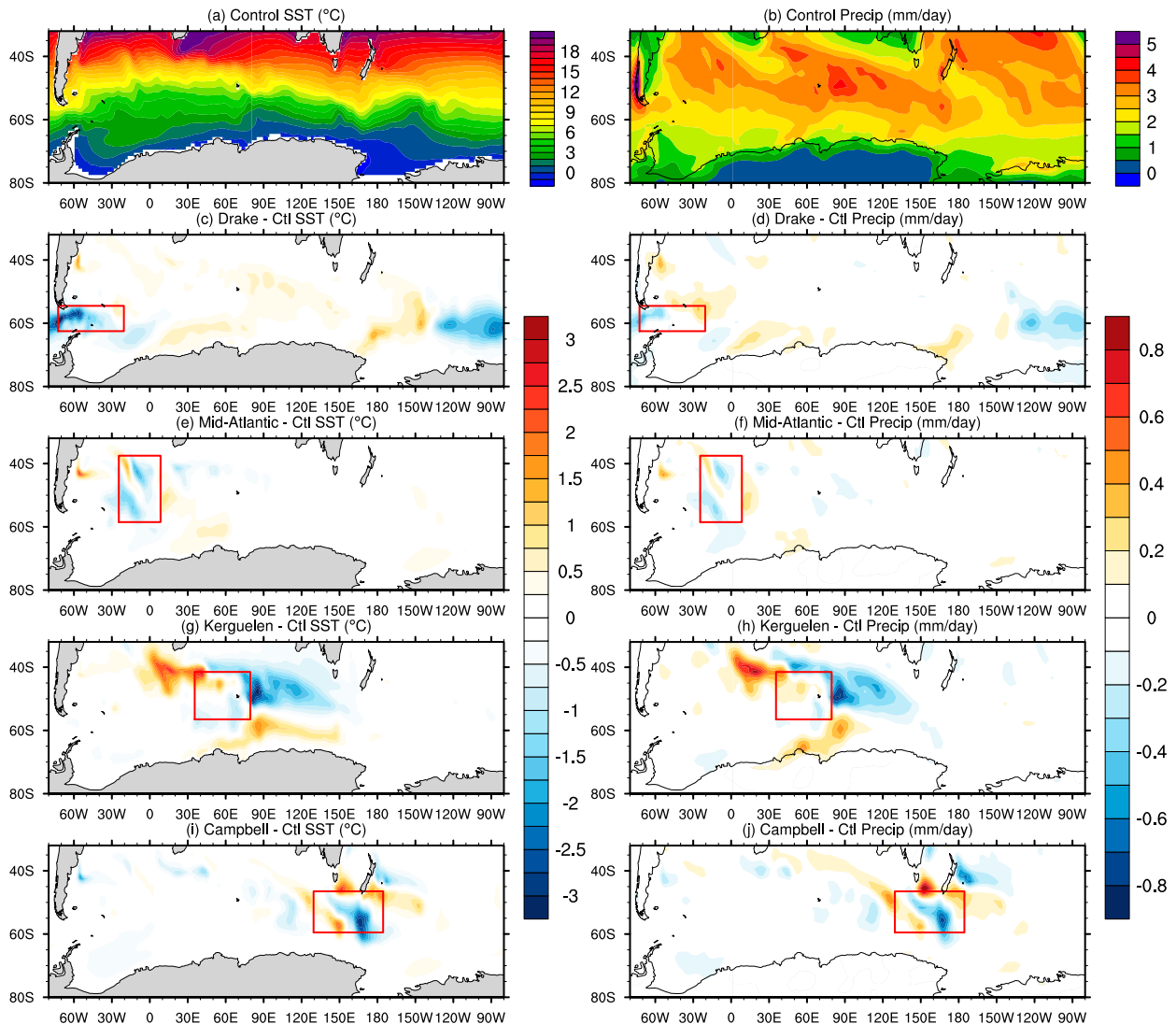
FIG. 4. (left) SST (°C) and (right) precipitation (mm day^{-1}) in the (a),(b) control, and (c)–(j) anomalies from the control for the four perturbation experiments. Red boxes show the regions where barriers were removed.

averaged over the last 100 years of the simulation. In the perturbation experiments, there are noticeable changes in MLD in the Weddell Gyre and Ross Gyre regions, as well as south of the Kerguelen Plateau (Figs. 6c,e,g,i). To distinguish between a robust impact of the barriers compared to natural multidecadal to centennial variability, we investigate the time series of MLD (Fig. 7) at the five locations indicated with stars in Fig. 6a. These correspond to the two locations of maximum

MLD in the Weddell and Ross Seas in the Control simulation (68°S, 30°W and 70°S, 180°W), the two western edges of these regions of enhanced MLD (66°S, 0°W and 70°S, 150°W), and finally the location where the MLD is most enhanced in the Kerguelen experiment (65°S, 70°E).

In the Weddell Sea, the MLDs are not consistently different from each other in the experiments, either at the center or western point (Figs. 7a,b). For example, while the MLD is

TABLE 2. The mean ACC transport (in Sv) in the control simulation and the sensitivity experiments, the percentage change from the control in the sensitivity experiments, and the minimum to maximum transport with the range in parentheses. All values are for the last 300 years of the simulation (i.e., 1200–1500 years).

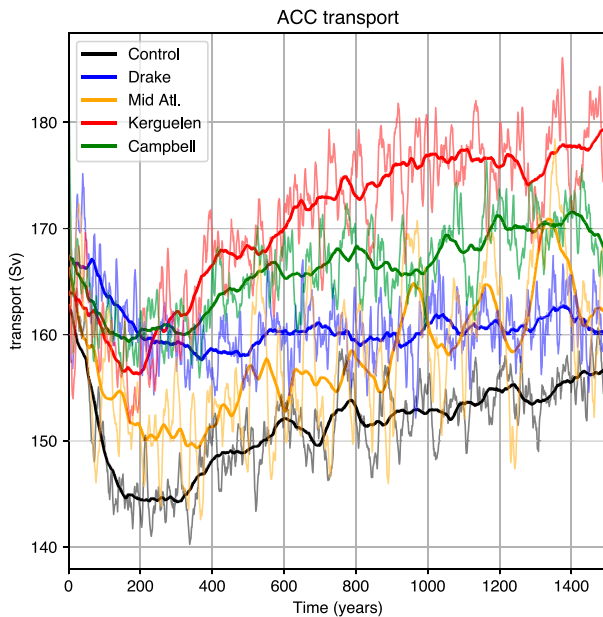| Case	Control	Drake	Mid-Atlantic	Kerguelen	Campbell	All flat
ACC (Sv)	155	161	164	177	170	241
Change (%)	—	4	6	14	10	56
Min–max (range) (Sv)	146–163 (17)	149–171 (22)	145–180 (34)	165–187 (22)	163–177 (14)	219–258 (39)

FIG. 5. Time series of ACC transports (in Sv) in the control and four perturbation experiments. Thin lines are 5-yr running averages, and the thick lines are 99-yr running averages.

deeper there in the Control simulation than in the perturbation experiments after 1500 years, this is not the case 200 or 400 years earlier in the simulations. The differences in the Weddell Sea MLD between the experiments seen over the last 100 years (Fig. 6) are therefore likely a result of random internal variability. In the Ross Sea it appears that the removal of the topographic barriers led to an increase in the MLD (Fig. 6) but the time series indicate again that most of this apparent signal is due to natural variability (Figs. 7d,e). One notable exception is at the point where the MLD is maximum in the Ross Sea in the control simulation; here the MLD reduces from ~600 to ~250 m in the Drake experiment around 800 years into the simulation (Fig. 7d). The relationship between the ocean circulation and deep convection is not obvious as the convection changes 800 years into the simulation while the ACC transport does not change at this time. On the eastern side of the Ross Sea, the natural variability is again larger than any differences between the experiments, although the MLD is somewhat more stable in the Drake experiment and does not reach the depths over 1500 m that is found in the 5-yr averaged MLDs in the other experiments (Fig. 7e). This is likely related to the fact that the Ross Gyre in the Drake experiment (Fig. 2) disappears in the Drake experiment (Fig. 2), but not in any of the other experiments. Indeed, earlier in the simulations (years 250–300), the strength of the Ross Gyre as well as the variability in its MLD are weaker in all simulations except the Drake experiment, in which both the gyre and the mean MLD across the Ross Sea are stronger (Figs. 7d,e; see also Fig. S2).

Finally, we investigate the apparent deepening of the MLD in the Indian Ocean sector of the Southern Ocean, when the Kerguelen Plateau is removed (Fig. 6g). This signal is indeed robust in the time series; in the Kerguelen experiment the MLD

here is ~1300 m deep, while the MLD hovers between 200 and 500 m in the other experiments (Fig. 7c). The increased ventilation is also visible in a slightly enhanced bottom cell of the global overturning streamfunction, which increases by ~2 Sv (Fig. 6h). We do not find the warming in the Weddell Sea and reduced bottom cell reported by Wang et al. (2016), which may be because we also removed the Del Caño Rise and the Conrad Rise west of Kerguelen. This leads to a different dynamic in the Agulhas region where Indian Ocean exchange occur with the Atlantic and Southern Ocean and to which they attribute their deep circulation changes. Alternatively, it may be because we have a coupled model and our SST, surface salinity, and wind fields are free to adjust.

4. The impact of barriers on the atmosphere

a. Precipitation

As seen in the previous section, the removal of the barriers leads to a zonal flattening of the SST contours and thus SST anomalies above and up and downstream of where the barriers are in the Control. Here we investigate the feedback of the SST anomalies on precipitation. A direct link between SST and convective activity in the atmosphere has been established in midlatitude warm western boundary regions (Czaja and Blunt 2011; de Boer et al. 2013a) and in the tropics (He et al. 2018). In general, the correlation between monthly time series of SST and precipitation, in both observations and CMIP5 models, is higher in areas over warmer waters but it does not follow the SST climatology directly. For instance, the correlation is highest over the western equatorial warm pool but small over some parts of the warm pool and even negative in some areas in the subtropics (He et al. 2018). Establishing the influence of SST on precipitation is challenging in coupled models because a large part of the atmospheric variability, especially on monthly time scales, is not forced by SST but instead impacts the ocean response (He et al. 2017). In this study, the SST anomalies between the experiments are from long-term averages and a result of bathymetrically driven ocean transport changes, since these are the only differences in forcing between the experiments. The precipitation anomalies can therefore be directly linked to the SST changes.

We find a striking coupling between the SST anomalies and the precipitation anomalies in all four experiments (Fig. 4). The coupling is evident in the whole domain, stretching from 33°S to the Antarctic coast. The spatial correlations between the SST and precipitation anomalies (where ΔSST $> 0.5°$C), calculated from the time-averaged final 100 years of the simulations, are $r = 0.92$, 0.97, 0.96 and 0.94 for the Drake, Mid-Atlantic, Kerguelen, and Campbell experiments respectively. The regression coefficients in each case are 0.16, 0.20, 0.25 and 0.26 mm day^{-1} °C^{-1} respectively, with an average of 0.22 mm day^{-1} °C^{-1}. The correlations are somewhat reduced when applying a lower or no threshold but does not drop below $r = 0.8$ for any simulation (Table S1). The link between the precipitation increase and the SST increase can be attributed to SST-induced increases in evaporation, as both the patterns and magnitude of the precipitation and evaporation anomalies
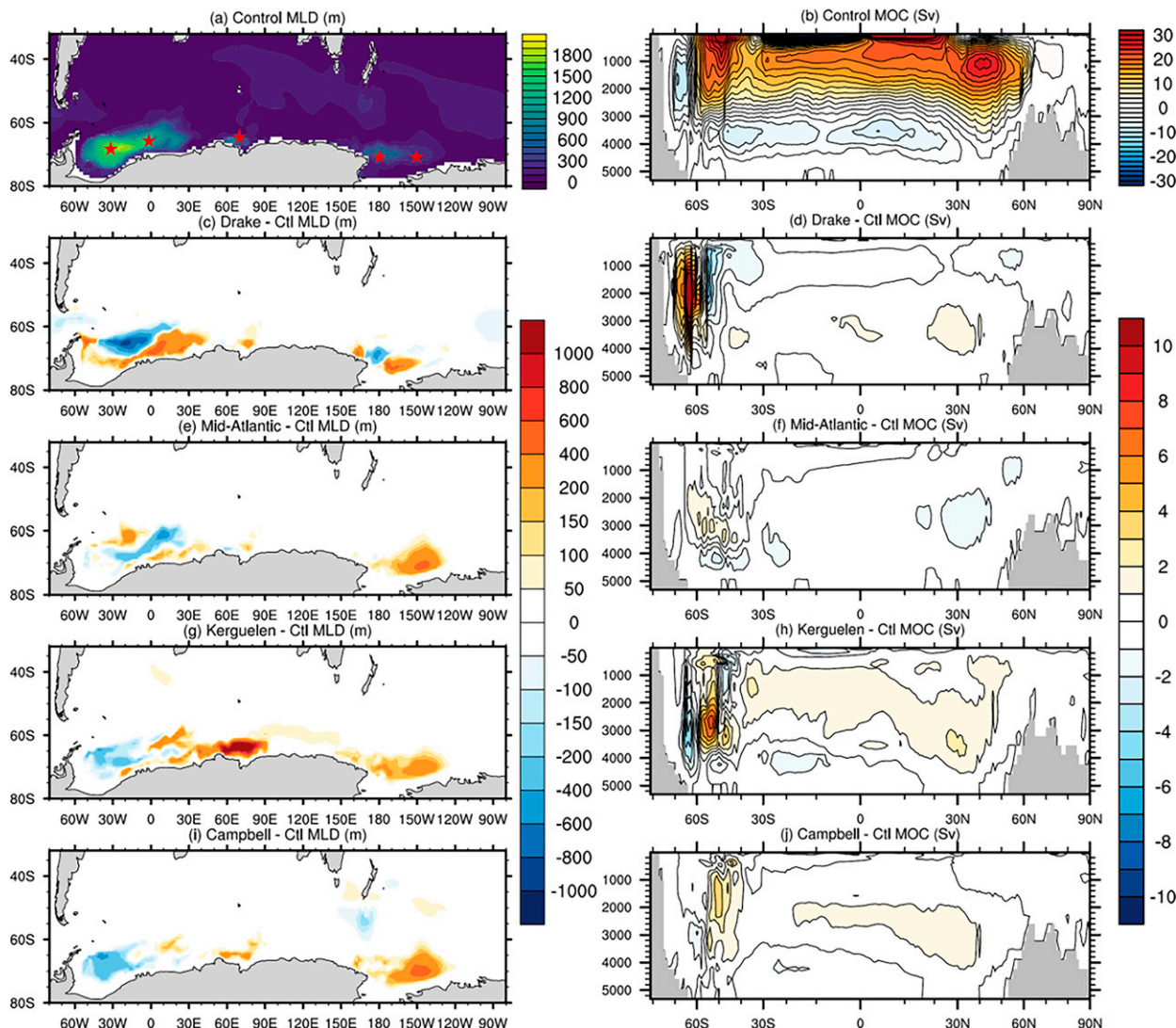
FIG. 6. (a) The MLD (m) and (b) global meridional overturning streamfunction (Sv) averaged over the last 100 years of the control simulation. The subsequent four rows are the (c),(e),(g),(i) MLD and (d),(f),(h),(j) streamfunction anomalies from the control for the four perturbation experiments. Contour intervals of the streamfunctions are 2 Sv in (a) and 1 Sv in (d), (f), (h), and (j). Red stars indicate the locations of the time series in Fig. 7.

in the simulations are remarkably similar (Fig. 8). The result is robust, as demonstrated by very similar evaporation anomalies when averaging over the preceding 100 years of the simulation (Fig. S3). The changes in precipitation as a result of the bathymetric changes are about 10%–30% relative to that in the control simulation (calculated, but not shown here). These results suggest a role for bathymetry, even in the deep ocean, in controlling the distribution of precipitation over the Southern Ocean.

b. Wind

Winds in the Southern Ocean are thought to drive the upwelling branch of the deep circulation (de Boer et al. 2008; Toggweiler and Samuels 1995) and impact carbon storage in the ocean (Le Quéré et al. 2007; Toggweiler 1999). Models predict a strengthening and southward shift of the westerly

wind jet under future warming scenarios (Bracegirdle et al. 2013) although the response of the winds to warming in general is dependent on the background state and in particular the sea ice edge (Sime et al. 2016). The position and strength of the westerlies have also been coupled to extratropical SSTs (Marshall and Connolley 2006) and its wavenumber-3 structure attributed to the continental configuration in the tropics (Goyal et al. 2021). Here we focus on the role of the Southern Ocean topographic barriers (via SST) on the local winds, the overall zonal asymmetry of the sea level pressure (SLP) driving the westerly jet, and the zonal asymmetry in the wind stress curl.

1) WIND SPEED

The relationship between SST and overlying wind strength, where colder water tends to damp the wind speed more
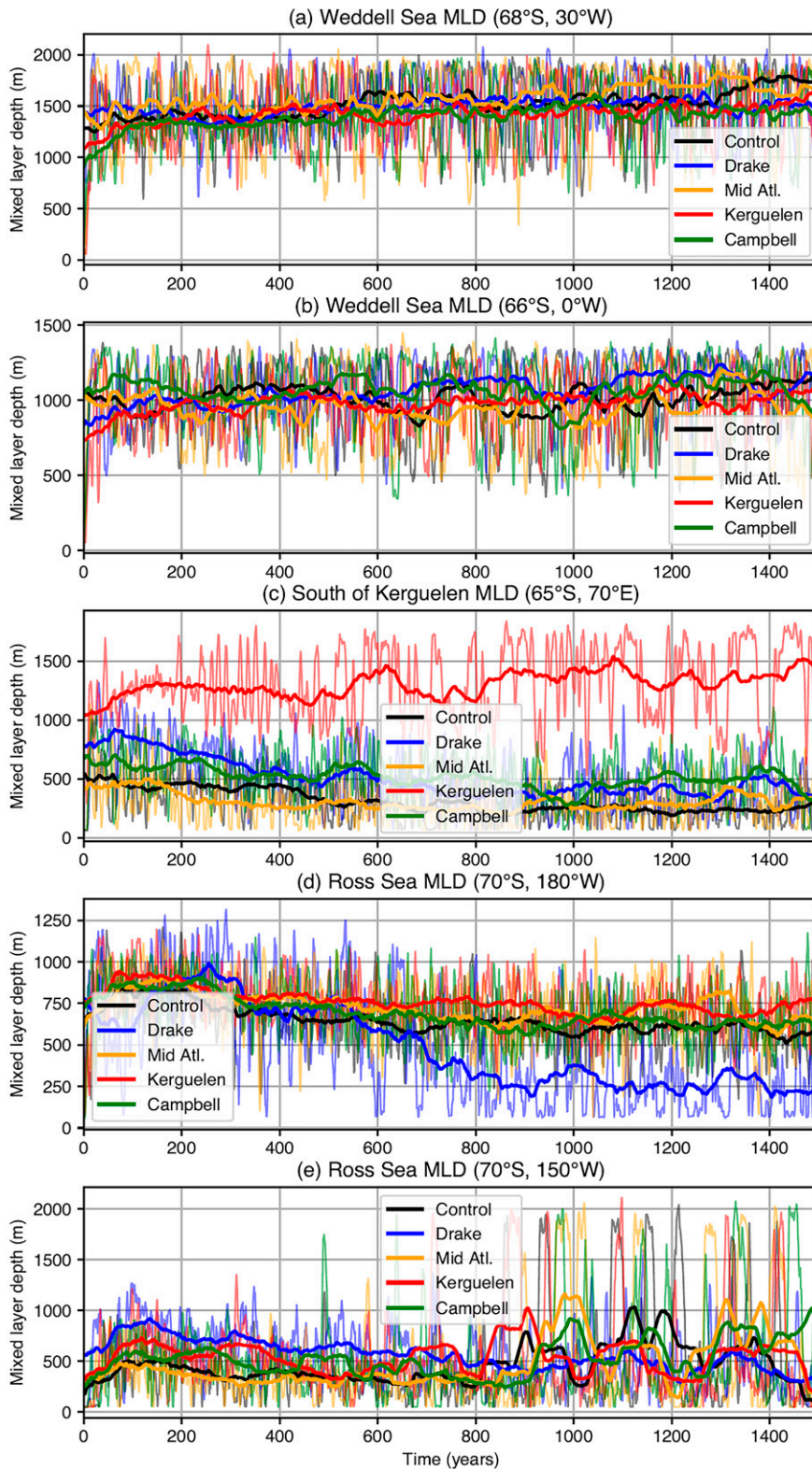
FIG. 7. Time series of MLD in the locations indicated with red stars in Fig. 6a. Thick lines show the 99-yr running average while the thin lines show the 5-yr running average.
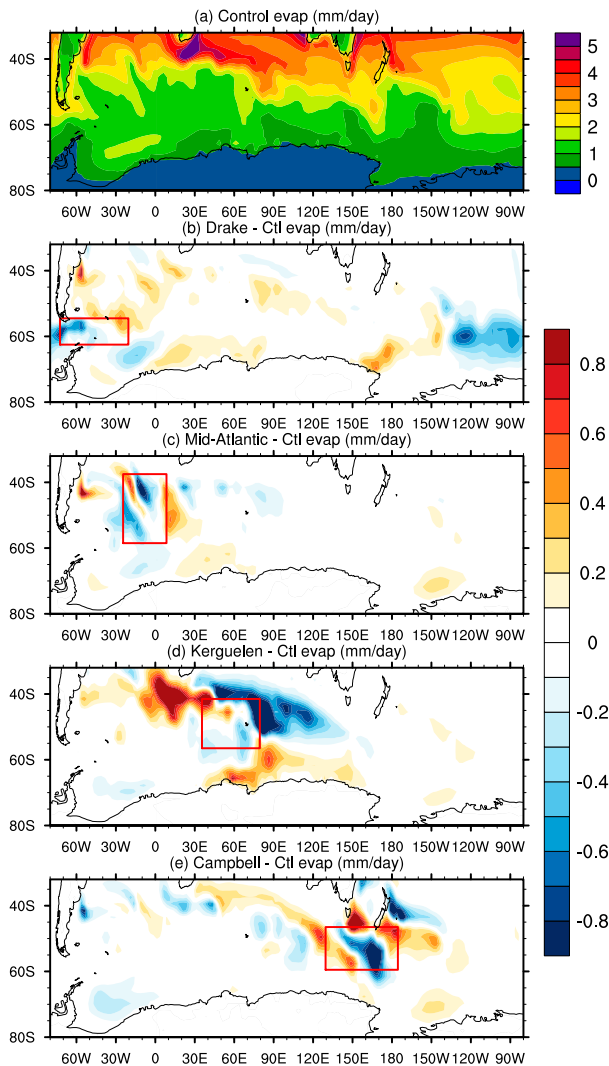
FIG. 8. (a) Evaporation (mm day^{-1}) in the control simulation, and (b)–(e) anomalies from the control simulation in the four experiments. Red boxes show where barriers were removed.

(Chelton et al. 2004; Small et al. 2008), is clearly visible in the Mid-Atlantic and Campbell experiments. In these two experiments the SST anomalies are mostly confined to the locations where the barriers are removed. The cold SST anomalies in the perturbation experiments (Fig. 4, left) correspond to reduced surface winds (Figs. 9f,j) and warm SST anomalies correspond to increased winds. This is also corroborated quantitatively in the Mid-Atlantic and Campbell experiments where the correlations between the SST anomalies (where $\Delta SST > 0.5°C$) and the wind speed differences are $r = 0.86$ and $r = 0.70$ respectively, with corresponding regression coefficients of 0.16 and 0.13 m s^{-1} °C^{-1}. However, this robust connection breaks down in the Drake and Kerguelen experiments where the correlations between SST and wind anomalies are merely 0.18 and 0.32, respectively, and it also breaks down when no threshold is used for temperature changes (Table S1). In the Kerguelen experiment there is still a qualitative relation visible as the

warming–cooling–warming pattern from northwest to southeast over the Kerguelen Plateau region (Fig. 4g) corresponds to a similar weakening–strengthening–weakening pattern in the surface winds anomalies (Fig. 9h). However, in the Drake experiment there is no obvious relationship between the SST and wind anomalies. There the strongest cooling upstream of Drake Passage and on its northern flank is not accompanied by a pattern of weaker winds. Instead, the winds weaken directly west of South America and intensify downstream of Drake Passage.

The SST anomalies produce local SLP anomalies that are broadly anticorrelated to them (Figs. 4, 9). For example, in the Drake experiment, there is a positive SLP anomaly over the cold region in and upstream of Drake Passage; in the Mid-Atlantic experiment, there is a positive SLP anomaly over the Mid-Atlantic ridge which is colder on average; in the Kerguelen experiment there are two negative SLP anomalies between South Africa and the Antarctic coast (~60°–120°E) and a positive SLP anomaly southwest of Australia corresponding to temperature anomalies of the opposite sign; finally in the Campbell experiment where is a positive SLP anomaly over the cold region south of New Zealand. These locally driven SLP anomalies incite a wave train around the Southern Ocean, creating a series of SLP highs and lows that is particularly clear in the Mid-Atlantic experiment (Fig. 9e). While the wind anomalies at the surface are a combination of the frictional effect of SST and the SLP anomalies, the winds farther aloft, at 925, 850, and 700 hPa, follow the SLP anomalies more closely in a geostrophic fashion (Fig. 9, left; see also Figs. S4–S6). The absolute strength of the wind speed anomalies is similar at these heights, but becomes smaller compared to the stronger mean flow aloft. The incited upstream and downstream changes in the winds (which are not a result of underlying SST changes) also mean that the correlations between the wind speed and the SST breaks down when no threshold is used for ΔSST (Table S1). Finally, we note that the wind anomaly patterns of the last 100 years (Fig. 9) are consistent over the preceding 100 years apart from small changes in the magnitude of the anomalies (Fig. S7), suggesting that they are robust features associated with the removal of the barriers, rather than natural multidecadal to centennial variability.

2) WESTERLY WIND JET

The removal of the topographic barriers leads to more zonally symmetric SST contours and the SST field in turn affects the SLP and overlying winds. Here we investigate whether the Southern Ocean bathymetry, through this link, has an effect on the familiar quasi-stationary wave-3 pattern in the Southern Hemisphere westerlies (Raphael 2004). In the Northern Hemisphere, where two ocean basins are interrupted by two continents, the jet stream exhibits strong zonal asymmetry in a wave-2 pattern, although the main driver of the wavy nature of the jet stream is the orography (Broccoli and Manabe 1992; Hall and Visbeck 2002). Recently, Goyal et al. (2021) were the first to investigate the wave-3 pattern in the Southern Hemisphere westerlies and, surprisingly, found that it is not related to Southern Hemisphere continents or orography, but that the pattern is
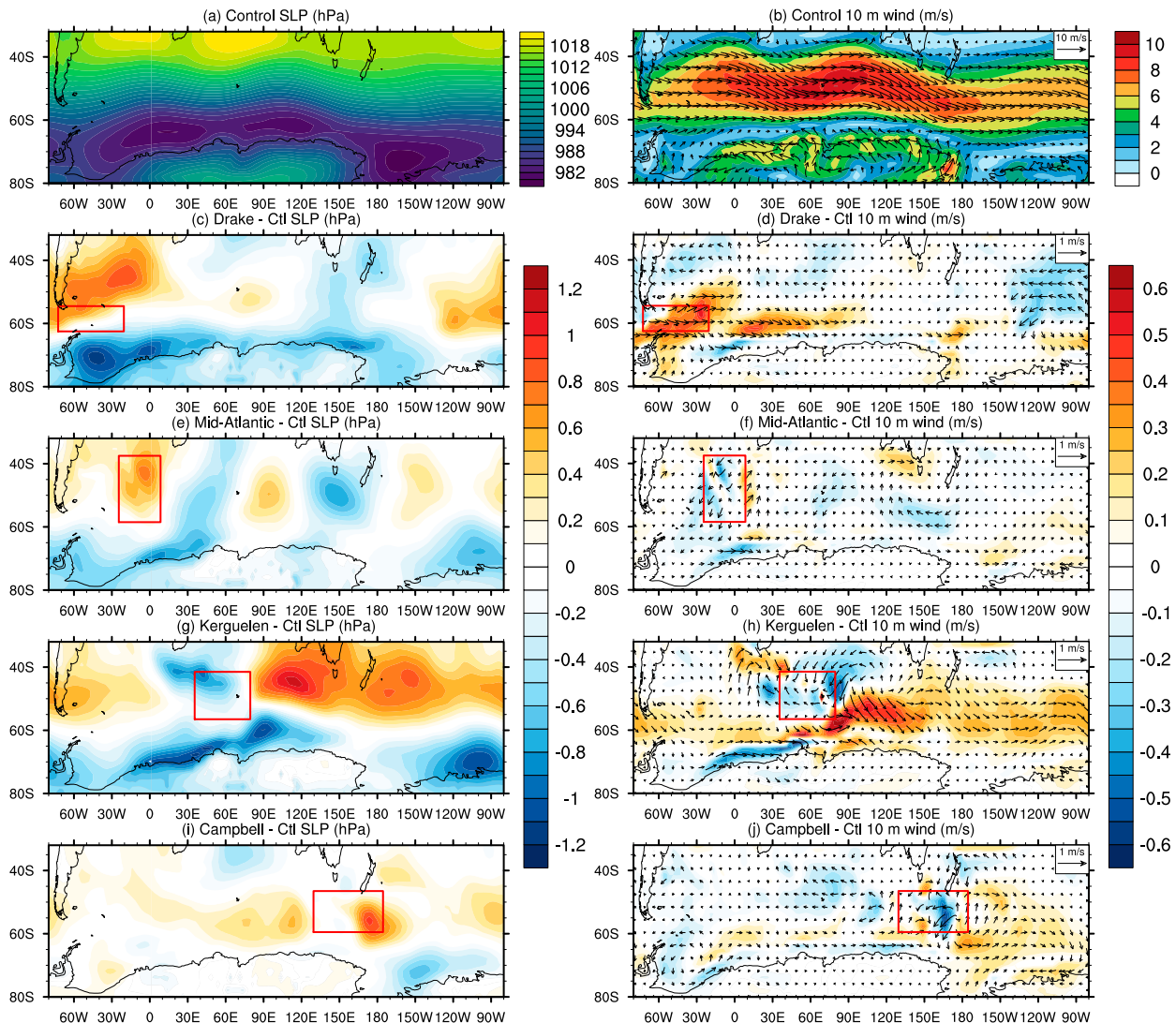
FIG. 9. (left) Sea level pressure (SLP) and (right) surface winds (10-m level) averaged over the last 100 years of the (a),(b) control simulation, and (c)–(j) the anomalies from the control in the four perturbation experiments for the same period. In the control simulation in (a) and (b), the color indicates the SLP (hPa) and the wind speed (m s^{-1}) and the arrows in the wind speed and direction. In the wind anomaly plots, the color indicates the difference of the wind speed and the arrows the difference in the wind velocity between the perturbation experiment and the control (m s^{-1}). Red boxes indicate where barriers were removed.

instead driven by zonal asymmetric deep atmospheric convection in the tropics.

We find no indication that the changes in SST anomalies in our perturbation experiments have any effect on the wave-3 pattern in the Southern Hemisphere midlatitude circulation (Fig. 10), consistent with Goyal et al. (2021). While the SST anomalies do produce a wavy pattern in the SLP anomalies (Fig. 9, left), these anomalies are only on the order of 1 hPa in a background field of winds driven by meridional SLP differences on the order of 30–40 hPa. Even when all four barriers are removed simultaneously, the SLP pattern remains similar (Fig. 10). Given that the orography plays a central role in setting up the asymmetry in the Northern Hemisphere westerlies, we performed three additional experiments in which the topography

was flattened over South America (the "Andes" experiment), Australia and New Zealand (the "Aus NZ" experiment), and Antarctica (the "Antarc flat" experiment), from 30°S poleward in each case. The removal of the South American topography or the Australian/New Zealand topography leads only to minor shifts of 1°–3° in SLP and no change in the overall wave-3 pattern (Fig. S8). Removal of the Antarctic topography leads to an increase in the waviness upstream of Drake Passage. The mode-3 waviness can therefore not be attributed to bathymetry or orography in the Southern Hemisphere.

3) WIND STRESS CURL

The wind stress is derived from the surface winds so that the impact of the bathymetry on the wind stress field is very
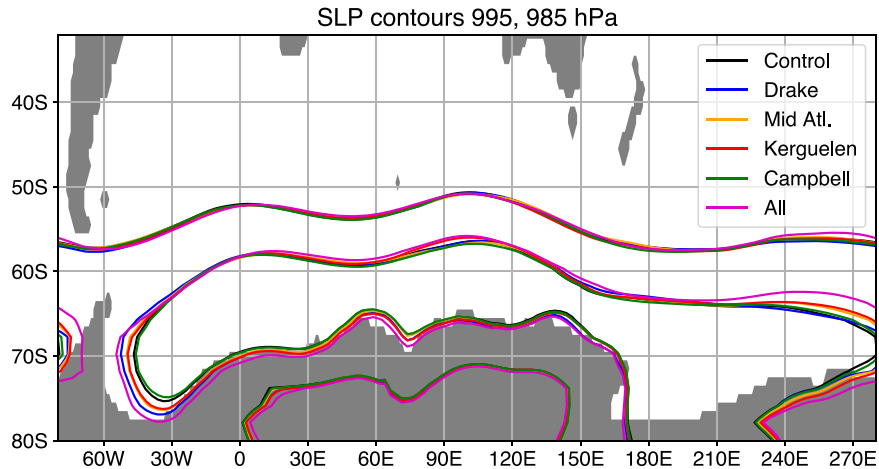
SLP contours 995, 985 hPa

FIG. 10. The 995- and 985-hPa SLP contours in the control simulation and the four main perturbation experiments. In addition, the SLP for an experiment call "All" is shown in which all barriers of the four experiments are removed simultaneously.

similar to its impact on the surface winds (not shown). The wind stress curl determines where the surface Ekman transport is divergent or convergent and the zero wind stress curl contour roughly separates upwelling and downwelling regions in the ocean. Further, the zero wind stress curl has frequently been associated with the subtropical front and the southern boundary of the subtropical gyre in the Atlantic (Beal et al. 2011; Biastoch et al. 2009). Although the zero wind stress curl lies in reality 5°–10° south of the subtropical front (de Boer et al. 2013b), it has been shown that strong SST meridional gradients across fronts can lead to a local flattening of the meridional gradient in the winds and wind stress, and thus to a reduced or zero wind stress curl (Graham et al. 2012; Pauthenet et al. 2017). One might therefore anticipate some local shifts in the zero wind stress curl contour as the fronts are shifted by the bathymetric features. A local shift in the wind is evident in the Mid-Atlantic experiment, since all other experiments exhibit a northward excursion of the zero wind stress curl contour at the Mid-Atlantic Ridge, but not when the bathymetry is flattened (Fig. 11). It is therefore clear that what appears to be random wiggles in the zero wind stress curl contour in the South Atlantic are in fact influenced by the bathymetry, through its impact on SST. In the Kerguelen experiment, the zero wind stress contour also loses much of its longitudinal variability around the barriers when they are removed (Fig. 11). Similarly, the removal of the Campbell Plateau flattens out meridional variability in the zero wind stress curl, which now migrates smoothly poleward from 120°E to 180° (Fig. 11). The zero wind stress curl is not impacted by the removal of barriers in the Drake experiment, which may be because the main jet of the Southern Hemisphere westerlies flows north of Drake Passage (Figs. 9 and 11). South of the maximum in the wind jet, the wind response can be diagnosed by the -6×10^{-8} N m^{-3} wind stress curl contour and this shows again the zonal smoothing of
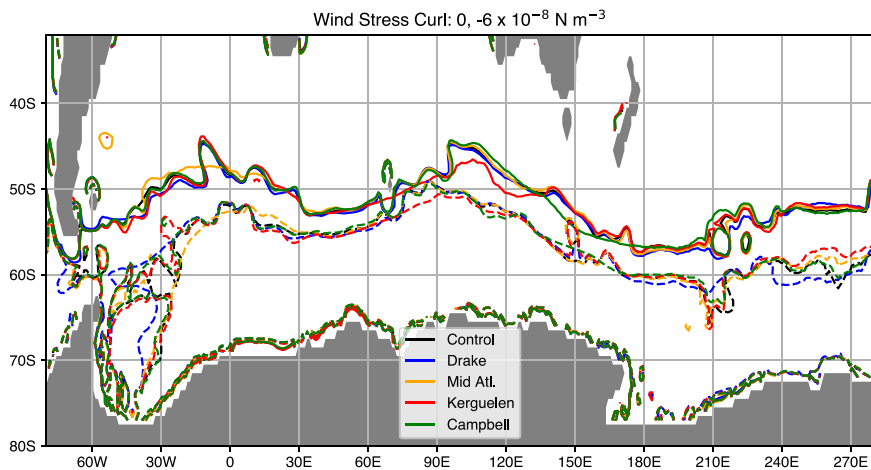
Wind Stress Curl: 0, -6 x 10^{-8} N m^{-3}

FIG. 11. Wind stress curl contours of 0 N m^{-3} (northern set) and -6×10^{-8} N m^{-3} (southern set) in the control and the four perturbation experiments.

meridional variability in the wind stress curl, by removal of the barriers in the Mid-Atlantic, Kerguelen, and Campbell experiments. However, in the region of the barriers that were removed in the Drake experiment, the wind stress curl is not consistent between the simulations, making it more difficult to compare the Drake experiment with the others. Nevertheless, some degree of zonal flattening is visible in this contour over the barriers north of 60°S and between 60° and 20°W.

5. Discussion and conclusions

We have investigated how the flow in the ACC is impacted by the removal of four major underwater topographic obstacles and how the SST field and overlying winds and precipitation are affected. As expected, with the removal of the barriers, the fronts and isotherms in the ACC becomes more zonal. However, the removal of the barriers downstream of Drake Passage does not result in the ACC flowing straight east after the passage. The proportion that flows northward after Drake Passage in the Malvinas Current remains similar (just slightly weaker). This is because the current normally deflects northward, not to avoid the barriers downstream of Drake Passage, but because of the strong wind stress around 50°S which drives the current (Allison et al. 2010). In the other three perturbation experiments, the flow crosses the barriers zonally, where it previously veered around it. Where a northeastward flow deflection in the control is more zonal in the perturbation experiment, the water becomes anomalously warmer (as the area is not fed by cold water from the south any longer). Similarly, where a southeastward deflection flattens out, the water becomes colder.

The removal of the individual barriers leads to an increase in the ACC transports ranging from a minimum of 6 Sv (4%) in the Drake experiment to maximum of 22 Sv (14%) in the Kerguelen experiment. When all four barriers are removed simultaneously, the ACC transport goes up by 86 Sv (56%), which is markedly more than the sum of the increases in the individual experiments (which is 34%). This is because the form stress that each barrier bears will increase as the barriers become less, and thus their removal will increasingly have a larger impact. The form stress redistribution occurs within the first year and the subsequent ACC variability is a result of the baroclinic forcing from the changing meridional density gradient caused by the adjustment of the stratification as the model is reaching an equilibrium (Wang et al. 2016). By the end of the 1500 years, the largest transport is found in the Kerguelen experiment, which also features a new region of deep convection to the south of the plateau, as well as a slight strengthening of the bottom overturning cell.

The topographic barriers also affect open ocean convection and Southern Ocean bottom water formation. We chose to investigate primarily MLD as an indication of bottom water formation, given that the more traditionally used global overturning streamfunction is a zonal sum of meridional transports in different ocean basins that originate from multiple northern and southern source regions. In the Weddell Sea and the eastern Ross Sea, the differences between the final

(100-yr average) MLD in the five experiments are of the same order as their multidecadal to centennial variability, suggesting that the barriers do not significantly affect convection here. However, two robust impacts of the barriers are found elsewhere. First, the removal of the barriers in the Drake experiment leads to a reduction in AABW formation formed upstream of Drake Passage in the western Ross Sea region. Second, the flattening of the bathymetry in the region of the Kerguelen Plateau greatly enhances the MLD south of the plateau, from ~300 m in the Control to 1400 m. We note that modern-day AABW formation happens mostly along the continental shelves in the real ocean and not in these large MLD regions that are found in the majority of global climate models (Heuzé 2021). However, observations do suggest that open-ocean deep convection used to be the main contributor to AABW formation prior to the 1950s (Broecker et al. 1999); whether the current cessation of open-ocean deep convection is part of the slow Atlantic seesaw (Broecker et al. 1999) or a consequence of ongoing climate change (de Lavergne et al. 2014) remains to be determined. Nevertheless, the results here may be relevant in so far as AABW formed on shelves may have an easier path to the bottom in a less stratified ocean.

The experiments in this study offer a unique chance to investigate the influence of the ocean SST on the atmosphere. In regular coupled model simulations, natural atmospheric variability perturbs the ocean SST, which in turn obscures the impact of the ocean variability on the atmosphere (He et al. 2017). Here, the natural variability is averaged out in the 100-yr-mean final state so that difference in wind and precipitation between the simulations can be directly attributed to changes in the ocean resulting from the SST through the bathymetry changes. We find a positive correlation between SST and local precipitation with the coefficient ranging from 0.92 to 0.97. The regression coefficient ranges from 0.16 to 0.26 mm day^{-1} °C^{-1}. While highly significant, the effect of the SST on the precipitation is weaker than in the tropics. In the tropics, the pointwise regression coefficient of precipitation on SST in observations ranges from about 4 mm day^{-1} °C^{-1} in the west Pacific warm pool to zero or negative values near 30°N and 30°S (He et al. 2017).

The resolution in the atmospheric model is not high enough to capture the response of atmospheric fronts to the SST changes (Parfitt and Seo 2018). However, the major features of the SST and precipitation responses already emerge after a few decades, suggesting that the role of SST on the atmosphere could be studied in more detail through similar experiments utilizing shorter simulations in a higher-resolution atmosphere and ocean model. In particular, the SST and precipitation responses seen in Fig. 4 can already be identified in the simulation averages for years 10–20, years 40–50, and years 90–100 (Figs. S9–11, respectively). The correlations between the SST and precipitation are also already high for years 10–20 (order $r = 0.9$), although here the correlations decrease (to order $r = 0.4$ to $r = 0.7$) when not using the ΔSST > 0.5°C threshold (Table S1). The wind fields are more variable. The first-order response of the winds to the topography is already present at 20 years, in the sense that one could visually match the winds fields in the experiments at 10–20 years (Fig. S12) to the experiments of the final average wind fields (Fig. 9). However, there is also

considerable variability from decade to decade as can be seen by comparing the simulations at years 10–20, years 40–50, and years 90–100 (Figs. S12–14 respectively) and from the weak to insignificant correlations between the SST and the wind field for these periods (Table S1).

The SST also affects the speed of the overlying winds, and in particular cooler surface waters slow down the surface winds. We find a reasonable correlation between wind speed and SST of $r = 0.86$ and $r = 0.70$ in the Mid-Atlantic and Campbell experiments respectively, with corresponding regression coefficients of 0.16 and 0.13 m s^{-1} °C^{-1}. However, the correlation between SST and wind speed breaks down in the Drake and Kerguelen experiments. This is because the winds, especially aloft, are influenced by a circumpolar wave train of SLP deviations generated by the SST anomalies. The changes in SST brought about by the removal of the barriers are not large enough to affect the overall wave-3 structure of the Southern Hemisphere westerlies, even when all barriers are removed simultaneously. This pattern was also not affected by removing the orography in South America or Australia/New Zealand and was even exaggerated when removing the orography of Antarctica (Fig. 10). Therefore, unlike in the Northern Hemisphere, orography does not seem to play a major role in the zonal asymmetry of the Southern Hemispheric midlatitude circulation. These findings are consistent with the work of Goyal et al. (2021) in which they conclude that the wave-3 structure is primarily forced by the landmass and SST distribution in the tropics. Nevertheless, the zonally flatter structure in SST does flatten out local wind stress curl anomalies, suggesting that a local correspondence between wind stress curl and fronts is forced from the ocean rather than the atmosphere.

An important limitation of our experiments is that the ocean model has a relatively coarse resolution that does not resolve eddies. Wang et al. (2016) discussed the limitations of using a non-eddy-resolving model in the Southern Ocean for their study in which the Kerguelen Plateau was removed, suggesting that the role of the bottom topography on the surface is likely overestimated without eddies. At the same time, eddy-resolving models tend to be more barotropic than low-resolution models, which implies that the impact of bottom topography could be underestimated here (Kjellsson and Zanna 2017). The dynamics of the ACC, and in particular its sensitivity to wind stress variability, is known to depend on eddies through the process of eddy saturation (Marshall et al. 2017). This means that the amplitude of changes in ACC transport obtained here should be interpreted with caution. However, since the main driver for these changes is the redistribution of form stress and not variations in wind stress, it is reasonable to assume that at least the sign and relative amplitude of variations is correct. In all cases, the sensitivity experiments illuminate important couplings between SST, winds and precipitation that are robust features of the coupled ocean–atmosphere system in the Southern Ocean.

REFERENCES

Allison, L. C., H. L. Johnson, D. P. Marshall, and D. R. Munday, 2010: Where do winds drive the Antarctic Circumpolar Current? *Geophys. Res. Lett.*, **37**, L12605, https://doi.org/10.1029/2010GL043355.

Beal, L. M., and Coauthors, 2011: On the role of the Agulhas system in ocean circulation and climate. *Nature*, **472**, 429–436, https://doi.org/10.1038/nature09983.

Biastoch, A., C. W. Boning, F. U. Schwarzkopf, and J. R. E. Lutjeharms, 2009: Increase in Agulhas leakage due to poleward shift of Southern Hemisphere westerlies. *Nature*, **462**, 495–498, https://doi.org/10.1038/nature08519.

Bishop, S. P., P. R. Gent, F. O. Bryan, A. F. Thompson, M. C. Long, and R. Abernathey, 2016: Southern Ocean overturning compensation in an eddy-resolving climate simulation. *J. Phys. Oceanogr.*, **46**, 1575–1592, https://doi.org/10.1175/JPO-D-15-0177.1.

Bracegirdle, T. J., and Coauthors, 2013: Assessment of surface winds over the Atlantic, Indian, and Pacific Ocean sectors of the Southern Ocean in CMIP5 models: Historical bias, forcing response, and state dependence. *J. Geophys. Res. Atmos.*, **118**, 547–562, https://doi.org/10.1002/jgrd.50153.

Broccoli, A. J., and S. Manabe, 1992: The effects of orography on midlatitude Northern Hemisphere dry climates. *J. Climate*, **5**, 1181–1201, https://doi.org/10.1175/1520-0442(1992)005<1181:TEOOOM>2.0.CO;2.

Broecker, W. S., S. Sutherland, and T.-H. Peng, 1999: A possible 20th-century slowdown of Southern Ocean deep water formation. *Science*, **286**, 1132–1135, https://doi.org/10.1126/science.286.5442.1132.

Bryan, K., and L. J. Lewis, 1979: A water mass model of the World Ocean. *J. Geophys. Res. Oceans*, **84**, 2503–2517, https://doi.org/10.1029/JC084iC05p02503.

Cessi, P., 2019: The global overturning circulation. *Annu. Rev. Mar. Sci.*, **11**, 249–270, https://doi.org/10.1146/annurev-marine-010318-095241.

Chelton, D. B., M. G. Schlax, M. H. Freilich, and R. F. Milliff, 2004: Satellite measurements reveal persistent small-scale features in ocean winds. *Science*, **303**, 978–983, https://doi.org/10.1126/science.1091901.

Cheon, W. G., Y.-G. Park, J. R. Toggweiler, and S.-K. Lee, 2014: The relationship of Weddell polynya and open-ocean deep convection to the Southern Hemisphere westerlies. *J. Phys. Oceanogr.*, **44**, 694–713, https://doi.org/10.1175/JPO-D-13-0112.1.

Czaja, A., and N. Blunt, 2011: A new mechanism for ocean–atmosphere coupling in midlatitudes. *Quart. J. Roy. Meteor. Soc.*, **137**, 1095–1101, https://doi.org/10.1002/qj.814.

de Boer, A. M., J. R. Toggweiler, and D. M. Sigman, 2008: Atlantic dominance of the meridional overturning circulation. *J. Phys. Oceanogr.*, **38**, 435–450, https://doi.org/10.1175/2007JPO3731.1.

——, A. B. Collier, and R. Caballero, 2013a: Processes driving thunderstorms over the Agulhas Current. *J. Geophys. Res. Atmos.*, **118**, 2220–2228, https://doi.org/10.1002/jgrd.50238.

——, R. M. Graham, M. D. Thomas, and K. E. Kohfeld, 2013b: The control of the Southern Hemisphere westerlies on the position of the subtropical front. *J. Geophys. Res. Oceans*, **118**, 5669–5675, https://doi.org/10.1002/jgrc.20407.

de Lavergne, C., J. B. Palter, E. D. Galbraith, R. Bernardello, and I. Marinov, 2014: Cessation of deep convection in the open Southern Ocean under anthropogenic climate change. *Nat. Climate Change*, **4**, 278–282, https://doi.org/10.1038/nclimate2132.

Delworth, T. L., and Coauthors, 2006: GFDL's CM2 global coupled climate models. Part I: Formulation and simulation characteristics. *J. Climate*, **19**, 643–674, https://doi.org/10.1175/JCLI3629.1.

Dufour, C. O., and Coauthors, 2015: Role of mesoscale eddies in cross-frontal transport of heat and biogeochemical tracers in the Southern Ocean. *J. Phys. Oceanogr.*, **45**, 3057–3081, https://doi.org/10.1175/JPO-D-14-0240.1.

Elsworth, G., E. Galbraith, G. Halverson, and S. Yang, 2017: Enhanced weathering and CO_2 drawdown caused by latest Eocene strengthening of the Atlantic meridional overturning circulation. *Nat. Geosci.*, **10**, 213–216, https://doi.org/10.1038/ngeo2888.

Fyfe, J. C., and O. A. Saenko, 2005: Human-induced change in the Antarctic Circumpolar Current. *J. Climate*, **18**, 3068–3073, https://doi.org/10.1175/JCLI3447.1.

Gille, S. T., 1997: The Southern Ocean momentum balance: Evidence for topographic effects from numerical model output and altimeter data. *J. Phys. Oceanogr.*, **27**, 2219–2232, https://doi.org/10.1175/1520-0485(1997)027<2219:TSOMBE>2.0.CO;2.

Goldner, A., N. Herold, and M. Huber, 2014: Antarctic glaciation caused ocean circulation changes at the Eocene–Oligocene transition. *Nature*, **511**, 574–577, https://doi.org/10.1038/nature13597.

Goyal, R., M. Jucker, A. Sen Gupta, H. H. Hendon, and M. H. England, 2021: Zonal wave 3 pattern in the Southern Hemisphere generated by tropical convection. *Nat. Geosci.*, **14**, 732–738, https://doi.org/10.1038/s41561-021-00811-3.

Graham, R. M., and A. M. de Boer, 2013: The dynamical subtropical front. *J. Geophys. Res. Oceans*, **118**, 5676–5685, https://doi.org/10.1002/jgrc.20408.

——, ——, K. J. Heywood, M. R. Chapman, and D. P. Stevens, 2012: Southern Ocean fronts: Controlled by wind or topography? *J. Geophys. Res. Oceans*, **117**, C08018, https://doi.org/10.1029/2012JC007887.

Griffies, S. M., 1998: The Gent–McWilliams skew flux. *J. Phys. Oceanogr.*, **28**, 831–841, https://doi.org/10.1175/1520-0485(1998)028<0831:TGMSF>2.0.CO;2.

——, and Coauthors, 2005: Formulation of an ocean model for global climate simulations. *Ocean Sci.*, **1**, 45–79, https://doi.org/10.5194/os-1-45-2005.

Hall, A., and M. Visbeck, 2002: Synchronous variability in the Southern Hemisphere atmosphere, sea ice, and ocean resulting from the annular mode. *J. Climate*, **15**, 3043–3057, https://doi.org/10.1175/1520-0442(2002)015<3043:SVITSH>2.0.CO;2.

He, J., C. Deser, and B. J. Soden, 2017: Atmospheric and oceanic origins of tropical precipitation variability. *J. Climate*, **30**, 3197–3217, https://doi.org/10.1175/JCLI-D-16-0714.1.

——, N. C. Johnson, G. A. Vecchi, B. Kirtman, A. T. Wittenberg, and S. Sturm, 2018: Precipitation sensitivity to local variations in tropical sea surface temperature. *J. Climate*, **31**, 9225–9238, https://doi.org/10.1175/JCLI-D-18-0262.1.

Heuzé, C., 2021: Antarctic Bottom Water and North Atlantic Deep Water in CMIP6 models. *Ocean Sci.*, **17**, 59–90, https://doi.org/10.5194/os-17-59-2021.

Hogg, A. M., 2010: An Antarctic Circumpolar Current driven by surface buoyancy forcing. *Geophys. Res. Lett.*, **37**, L23601, https://doi.org/10.1029/2010GL044777.

Hutchinson, D. K., A. M. de Boer, H. K. Coxall, R. Caballero, J. Nilsson, and M. Baatsen, 2018: Climate sensitivity and meridional overturning circulation in the late Eocene using GFDL CM2.1. *Climate Past*, **14**, 789–810, https://doi.org/10.5194/cp-14-789-2018.

——, H. K. Coxall, M. O'Regan, J. Nilsson, R. Caballero, and A. M. de Boer, 2019: Arctic closure as a trigger for Atlantic overturning at the Eocene–Oligocene transition. *Nat. Commun.*, **10**, 3797, https://doi.org/10.1038/s41467-019-11828-z.

——, and Coauthors, 2021: The Eocene–Oligocene transition: A review of marine and terrestrial proxy data, models and model–data comparisons. *Climate Past*, **17**, 269–315, https://doi.org/10.5194/cp-17-269-2021.

Inatsu, M., and B. J. Hoskins, 2004: The zonal asymmetry of the Southern Hemisphere winter storm track. *J. Climate*, **17**, 4882–4892, https://doi.org/10.1175/JCLI-3232.1.

Johnson, G. C., and H. L. Bryden, 1989: On the size of the Antarctic Circumpolar Current. *Deep-Sea Res.*, **36A**, 39–53, https://doi.org/10.1016/0198-0149(89)90017-4.

Katz, M. E., and Coauthors, 2011: Impact of Antarctic Circumpolar Current development on late Paleogene ocean structure. *Science*, **332**, 1076–1079, https://doi.org/10.1126/science.1202122.

Killworth, P. D., and C. W. Hughes, 2002: The Antarctic Circumpolar Current as a free equivalent-barotropic jet. *J. Mar. Res.*, **60**, 19–45, https://doi.org/10.1357/002224002762341230.

Kjellsson, J., and L. Zanna, 2017: The impact of horizontal resolution on energy transfers in global ocean models. *Fluids*, **2**, 45, https://doi.org/10.3390/fluids2030045.

Langlais, C. E., S. R. Rintoul, and J. D. Zika, 2015: Sensitivity of Antarctic Circumpolar Current transport and eddy activity to wind patterns in the Southern Ocean. *J. Phys. Oceanogr.*, **45**, 1051–1067, https://doi.org/10.1175/JPO-D-14-0053.1.

Le Quéré, C., and Coauthors, 2007: Saturation of the Southern Ocean CO_2 sink due to recent climate change. *Science*, **316**, 1735–1738, https://doi.org/10.1126/science.1136188.

Marshall, D., 1995: Topographic steering of the Antarctic Circumpolar Current. *J. Phys. Oceanogr.*, **25**, 1636–1650, https://doi.org/10.1175/1520-0485(1995)025<1636:TSOTAC>2.0.CO;2.

——, M. H. P. Ambaum, J. R. Maddison, D. R. Munday, and L. Novak, 2017: Eddy saturation and frictional control of the Antarctic Circumpolar Current. *Geophys. Res. Lett.*, **44**, 286–292, https://doi.org/10.1002/2016GL071702.

Marshall, G. J., and W. M. Connolley, 2006: Effect of changing Southern Hemisphere winter sea surface temperatures on Southern Annular Mode strength. *Geophys. Res. Lett.*, **33**, L17717, https://doi.org/10.1029/2006GL026627.

Martin, T., W. Park, and M. Latif, 2013: Multi-centennial variability controlled by Southern Ocean convection in the Kiel Climate Model. *Climate Dyn.*, **40**, 2005–2022, https://doi.org/10.1007/s00382-012-1586-7.

Martinson, D. G., 2012: Antarctic Circumpolar Current's role in the Antarctic ice system: An overview. *Palaeogeogr.*

Palaeoclimatol. Palaeoecol., **335–336**, 71–74, https://doi.org/10.1016/j.palaeo.2011.04.007.

Masich, J., T. K. Chereskin, and M. R. Mazloff, 2015: Topographic form stress in the Southern Ocean state estimate. *J. Geophys. Res. Oceans*, **120**, 7919–7933, https://doi.org/10.1002/2015JC011143.

Murray, R. J., 1996: Explicit generation of orthogonal grids for ocean models. *J. Comput. Phys.*, **126**, 251–273, https://doi.org/10.1006/jcph.1996.0136.

Newsom, E. R., A. F. Thompson, J. F. Adkins, and E. D. Galbraith, 2021: A hemispheric asymmetry in poleward ocean heat transport across climates: Implications for overturning and polar warming. *Earth Planet. Sci. Lett.*, **568**, 117033, https://doi.org/10.1016/j.epsl.2021.117033.

Parfitt, R., and H. Seo, 2018: A new framework for near-surface wind convergence over the Kuroshio Extension and Gulf Stream in wintertime: The role of atmospheric fronts. *Geophys. Res. Lett.*, **45**, 9909–9918, https://doi.org/10.1029/2018GL080135.

Patmore, R. D., P. R. Holland, D. R. Munday, A. C. Naveira Garabato, D. P. Stevens, and M. P. Meredith, 2019: Topographic control of Southern Ocean gyres and the Antarctic Circumpolar Current: A barotropic perspective. *J. Phys. Oceanogr.*, **49**, 3221–3244, https://doi.org/10.1175/JPO-D-19-0083.1.

Pauthenet, E., F. Roquet, G. Madec, and D. Nerini, 2017: A linear decomposition of the Southern Ocean thermohaline structure. *J. Phys. Oceanogr.*, **47**, 29–47, https://doi.org/10.1175/JPO-D-16-0083.1.

Raphael, M. N., 2004: A zonal wave 3 index for the Southern Hemisphere. *Geophys. Res. Lett.*, **31**, L23212, https://doi.org/10.1029/2004GL020365.

Rintoul, S. R., 2018: The global influence of localized dynamics in the Southern Ocean. *Nature*, **558**, 209–218, https://doi.org/10.1038/s41586-018-0182-3.

Shi, J.-R., L. D. Talley, S.-P. Xie, W. Liu, and S. T. Gille, 2020: Effects of buoyancy and wind forcing on Southern Ocean climate change. *J. Climate*, **33**, 10 003–10 020, https://doi.org/10.1175/JCLI-D-19-0877.1.

Sijp, W. P., M. H. England, and M. Huber, 2011: Effect of the deepening of the Tasman Gateway on the global ocean. *Paleoceanography*, **26**, PA4207, https://doi.org/10.1029/2011PA002143.

Sime, L. C., K. E. Kohfeld, C. Le Quéré, E. W. Wolff, A. M. de Boer, R. M. Graham, and L. Bopp, 2013: Southern Hemisphere westerly wind changes during the Last Glacial Maximum: Model–data comparison. *Quat. Sci. Rev.*, **64**, 104–120, https://doi.org/10.1016/j.quascirev.2012.12.008.

——, D. Hodgson, T. J. Bracegirdle, C. Allen, B. Perren, S. Roberts, and A. M. de Boer, 2016: Sea ice led to poleward-shifted winds at the Last Glacial Maximum: The influence of state dependency on CMIP5 and PMIP3 models. *Climate Past*, **12**, 2241–2253, https://doi.org/10.5194/cp-12-2241-2016.

Small, R. J., and Coauthors, 2008: Air–sea interaction over ocean fronts and eddies. *Dyn. Atmos. Oceans*, **45**, 274–319, https://doi.org/10.1016/j.dynatmoce.2008.01.001.

Sokolov, S., and S. R. Rintoul, 2007: On the relationship between fronts of the Antarctic Circumpolar Current and surface chlorophyll concentrations in the Southern Ocean. *J. Geophys. Res. Oceans*, **112**, C07030, https://doi.org/10.1029/2006JC004072.

Steele, M., R. Morley, and W. Ermold, 2001: PHC: A global ocean hydrography with a high-quality Arctic Ocean. *J. Climate*, **14**, 2079–2087, https://doi.org/10.1175/1520-0442(2001)014<2079:PAGOHW>2.0.CO;2.

Stevens, D. P., and V. O. Ivchenko, 1997: The zonal momentum balance in an eddy-resolving general-circulation model of the southern ocean. *Quart. J. Roy. Meteor. Soc.*, **123**, 929–951, https://doi.org/10.1002/qj.49712354008.

Taburet, G., and Coauthors, 2019: DUACS DT2018: 25 years of reprocessed sea level altimetry products. *Ocean Sci.*, **15**, 1207–1224, https://doi.org/10.5194/os-15-1207-2019.

Tansley, C. E., and D. P. Marshall, 2000: On the influence of bottom topography and the Deep Western Boundary Current on Gulf Stream separation. *J. Mar. Res.*, **58**, 297–325, https://doi.org/10.1357/002224000321511179.

——, and ——, 2001: On the dynamics of wind-driven circumpolar currents. *J. Phys. Oceanogr.*, **31**, 3258–3273, https://doi.org/10.1175/1520-0485(2001)031<3258:OTDOWD>2.0.CO;2.

Thompson, A. F., 2010: Jet formation and evolution in baroclinic turbulence with simple topography. *J. Phys. Oceanogr.*, **40**, 257–278, https://doi.org/10.1175/2009JPO4218.1.

Toggweiler, J. R., 1999: Variation of atmospheric CO_2 by ventilation of the ocean's deepest water. *Paleoceanography*, **14**, 571–588, https://doi.org/10.1029/1999PA900033.

——, and B. Samuels, 1995: Effect of Drake Passage on the global thermohaline circulation. *Deep-Sea Res. I*, **42**, 477–500, https://doi.org/10.1016/0967-0637(95)00012-U.

Toumoulin, A., Y. Donnadieu, J. B. Ladant, S. J. Batenburg, F. Poblete, and G. Dupont-Nivet, 2020: Quantifying the effect of the Drake Passage opening on the Eocene Ocean. *Paleoceanogr. Paleoclimatol.*, **35**, e2020PA003889, https://doi.org/10.1029/2020PA003889.

Viebahn, J. P., A. S. von der Heydt, D. Le Bars, and H. A. Dijkstra, 2016: Effects of Drake Passage on a strongly eddying global ocean. *Paleoceanography*, **31**, 564–581, https://doi.org/10.1002/2015PA002888.

Wang, J., M. R. Mazloff, and S. T. Gille, 2016: The effect of the Kerguelen Plateau on the ocean circulation. *J. Phys. Oceanogr.*, **46**, 3385–3396, https://doi.org/10.1175/JPO-D-15-0216.1.

Yang, S., E. Galbraith, and J. Palter, 2014: Coupled climate impacts of the Drake Passage and the Panama Seaway. *Climate Dyn.*, **43**, 37–52, https://doi.org/10.1007/s00382-013-1809-6.

Zhou, L., C. Heuzé, and M. Mohrmann, 2022: Early winter triggering of the Maud Rise polynya. *Geophys. Res. Lett.*, **49**, e2021GL096246, https://doi.org/10.1029/2021GL096246.

Zika, J. D., J. Le Sommer, C. O. Dufour, A. Naveira-Garabato, and A. Blaker, 2013: Acceleration of the Antarctic Circumpolar Current by wind stress along the coast of Antarctica. *J. Phys. Oceanogr.*, **43**, 2772–2784, https://doi.org/10.1175/JPO-D-13-091.1.